

Journal of Materials Chemistry A

Materials for energy and sustainability

Accepted Manuscript

This article can be cited before page numbers have been issued, to do this please use: J. Ma, F. Yu, T. Chen, J. Chen, S. Liang and P. Liu, *J. Mater. Chem. A*, 2026, DOI: 10.1039/D6TA02416E.



This is an Accepted Manuscript, which has been through the Royal Society of Chemistry peer review process and has been accepted for publication.

Accepted Manuscripts are published online shortly after acceptance, before technical editing, formatting and proof reading. Using this free service, authors can make their results available to the community, in citable form, before we publish the edited article. We will replace this Accepted Manuscript with the edited and formatted Advance Article as soon as it is available.

You can find more information about Accepted Manuscripts in the [Information for Authors](#).

Please note that technical editing may introduce minor changes to the text and/or graphics, which may alter content. The journal's standard [Terms & Conditions](#) and the [Ethical guidelines](#) still apply. In no event shall the Royal Society of Chemistry be held responsible for any errors or omissions in this Accepted Manuscript or any consequences arising from the use of any information it contains.

1 **Polyaminoanthraquinone with Modulated Iminium Electron**

2 **Delocalization for Efficient Electrochemical Ammonium**

3 **Removal**

4 Fei Yu^{1,3}, Tianjie Chen¹, Jinfeng Chen², Shuzhen Liang³, Peng Liu⁵, Jie Ma^{2,3,4*}

5 ¹ College of Oceanography and Ecological Science, Shanghai Ocean University,
6 No 999, Huchenghuan Road, Shanghai, 201306, P. R. China.

7 ² Research Center for Environmental Functional Materials, State Key Laboratory
8 of Water Pollution Control and Green Resource Recycling, College of Environmental
9 Science and Engineering, Tongji University, Shanghai, 200092, P. R. China.

10 ³ Water Resources and Water Environment Engineering Technology Center, Xinjiang
11 Key Laboratory of Engineering Materials and Structural Safety, School of Civil
12 Engineering, Kashi University, Kashi 844000, P. R. China.

13 ⁴ Shanghai Institute of Pollution Control and Ecological Security, Shanghai, 200092,
14 P.R. China

15 ⁵ Biolin (Shanghai) Trading Company Ltd, Rm 1205, Sandhill Plaza, Lane 2290
16 ZuChongzhi Road, Pudong New District, 201203 Shanghai China

17
18 Corresponding author: Jie Ma, E-mail: jma@tongji.edu.cn, Tel: +86-021-65981629



19 **Abstract**View Article Online
DOI: 10.1039/D6TA02416E

20 The development of organic electrode materials for capacitive deionization
21 (CDI) is hindered by limited redox-active sites and sluggish ion kinetics. Herein, a
22 proton-acid-mediated interfacial polymerization strategy is proposed to fabricate
23 nanoscale protonated polyaminoanthraquinone (PAAQ), mitigating these limitations.
24 The protonated imine groups (-NH-) on the PAAQ chains to form -NH₂⁺ polarons,
25 induces extensive π -electron delocalization along the polymer backbone, which
26 activates the latent redox sites and significantly boosts the electrochemical
27 performance. In addition, leveraging the intrinsically low crystallinity of PAAQ,
28 interfacial polymerization was coupled with agitation to disperse the aqueous oxidant
29 template, yielding nanoparticles whose increased specific surface area increases the
30 accessible active adsorption sites. The optimized PAAQ material delivers an
31 exceptional NH₄⁺ removal capacity of 120.43 mg g⁻¹ and a high rate of 9.22 mg g⁻¹
32 min⁻¹, surpassing most reported organic electrodes. The material also shows
33 outstanding cycling performance, maintaining 84.1 % of its original capacity after 50
34 CDI cycles. This work proposes a protonation-activated strategy that unlocks the
35 latent redox sites of conjugated polymers and amplifies their electrochemical
36 performance, providing valuable insights for the development of high-performance
37 organic electrodes in CDI and related energy storage applications.

38 **Keywords:** Capacitive deionization; Organic polymer; Ammonium removal; Water
39 purification; Electron delocalization

40



41 **1.Introduction**

42 With the expansion of agriculture, acceleration of industrialization, and population
43 growth, many ammonia nitrogen emissions caused ammonium ion (NH_4^+) pollution has
44 become one of the important environmental problems facing the world¹⁻³. Industrial activities,
45 including metallurgy, chemical manufacturing, fertilizer production, and coking, as well as
46 agricultural practices such as excessive use of fertilizers and discharge of livestock
47 wastewater, are the primary sources of ammonium nitrogen pollution^{4, 5}. The discharge of
48 wastewater containing ammonium nitrogen contributes to water eutrophication and leads to
49 the formation of hazardous substances such as nitrites and nitrates^{6, 7}. Ammonia reclaimed
50 from the environment is being re-envisioned as a strategic, renewable energy carrier,
51 capitalizing on its high energy density, carbon-free nature, safety, and transport
52 economy—benefits that go well beyond its historical use in fertilizers⁸⁻¹⁰. With a high
53 volumetric hydrogen density ($106 \text{ kg H}_2 \text{ m}^{-3}$ as a liquid at 300 K and 1.0 MPa, compared to
54 liquid hydrogen's $70 \text{ kg H}_2 \text{ m}^{-3}$ at 20 K)¹¹, ammonia is easy to store and transport, making it a
55 versatile medium. Thus, efficient ammonia recovery from aqueous environments holds
56 significant importance for environmental protection and energy utilization.

57 Traditional ammonia recovery methods, such as ammonia stripping, chemical
58 precipitation, oxidation, membrane filtration, biological treatment and so on, have
59 limitations^{12, 13}. Ammonia stripping needs pH and temperature adjustments, posing air
60 pollution and scaling risks. Struvite precipitation requires large amounts of magnesium and
61 alkali, yielding low fertilizer output. Anaerobic ammonium oxidation has a long start up
62 period and is sensitive to environmental changes. Therefore, there's an urgent need for a
63 pollution-free, cost-effective, and energy-efficient NH_4^+ capture technology. Capacitive
64 deionization (CDI) is an energy-saving emerging water treatment technology by adsorbing
65 ions onto electrodes under an applied DC voltage, which is easy to operate, sustainable, and
66 reusable with electrodes^{14, 15}. It can also selectively remove different ions through electrode
67 design^{16, 17}. Compared to the various limitations of traditional inorganic electrode materials,
68 such as anodic corrosion and co-ion effect of carbon materials, poor conductivity and volume



69 expansion of inorganic faraday materials¹⁸⁻²⁶, organic electrode materials, which achieve ion
70 storage through functional groups with redox activity to avoid the above defects, have become
71 a hot research topic in CDI electrode materials in recent years. This pseudocapacitive organic
72 electrode materials rich in active site such as carbonyl groups and Schiff bases have shown
73 significant advantages in high capacity, adjustability, stability, and low toxicity²⁷⁻³¹.

74 Given their high theoretical charge-storage capacities, well-defined redox potentials,
75 rapid kinetics, and structural diversity, quinones have been the subject of extensive
76 electrochemical research. Their theoretically substantial specific capacity is competitive with
77 lithium-ion systems^{32, 33}. 1-Aminoanthraquinone (AAQ), an inexpensive organic precursor
78 that incorporates redox-active quinone units, can be polymerized into extensively
79 π -conjugated architectures, thereby enhancing the overall charge density, which has been
80 widely exploited for proton storage and cation batteries. However, most previous CDI studies
81 have relied on quinone-based oligomers obtained through condensation reactions that aim to
82 establish a nominally complete π -conjugated backbone. The resulting polymer frameworks
83 are fragile and readily dissolved in flowing aqueous electrolytes, representing one of the
84 bottlenecks in the research of organic electrodes^{34, 35}. In fact, a straightforward
85 homopolymerization of AAQ directly affords a long-chain, robust polyaminoanthraquinone
86 (PAAQ) framework that withstands aqueous environments under periodic electric fields. Yet
87 this otherwise straightforward route has received scant attention because the homopolymer
88 backbone cannot sustain long-range π -electron delocalization, the majority of its redox-active
89 sites remain electrochemically silent. Although the anthraquinone moieties possess an
90 intramolecular π - π conjugated framework, the interunit p- π conjugation supplied by the
91 bridging imine group (-NH-) introduces periodic disruptions that act as energetic barriers to
92 electron delocalization along the PAAQ chains, leading to limited conductivity.

93 Recent investigations have demonstrated that protonation of these -NH- linkages by
94 protonic acids drives the formation of P-doped polaronic states that reorganize the charge
95 distribution along the PAAQ chain, and the resulting PAAQ effectively extends π -electron



96 delocalization across the entire conjugated architecture, thereby markedly enhancing
97 macroscopic electrical conductivity^{36, 37}. The improvement of conductivity is expected to
98 activate the redox sites on conjugated polymers to achieve higher electrochemical adsorption
99 capacity^{38, 39}. Additionally, In a reaction environment containing protonic acids, amino group
100 ($-\text{NH}_2$) are protonated to more reactive $-\text{NH}_3^+$, thereby promoting the continuous
101 polymerization of monomers to increase the yield of long-range polymers⁴⁰. It should also be
102 emphasized that monomers and oxidants are usually soluble in different solvents. Compared
103 with in-situ polymerization in a single solvent, interfacial polymerization in multiple solvents
104 usually achieves better results⁴¹. When two immiscible liquids form an interface, one of the
105 liquid solvents contains a monomer. Due to the difference in chemical potential between two
106 immiscible liquids at the interface, monomers can diffuse towards the interface and initiate
107 polymerization, thereby achieving precise design of the polymer structure based on solvent
108 soft templates.

109 In this work, a novel and convenient AAQ polymerization method was developed. By
110 utilizing the interface aggregation strategy and the promoting effect of proton acid, the
111 protonated PAAQ exhibits satisfactory microstructure and capacitance. This method achieves
112 an enhanced conductivity and activated redox sites for conjugated polymers by proton acid
113 regulation of electron delocalization, endowing them with excellent electrochemical
114 performance. At 1.2 V, the adsorption capacity of enhanced PAAQ for NH_4^+ is as high as
115 120.43 mg g^{-1} , and the adsorption rate is $9.22 \text{ mg g}^{-1} \text{ min}^{-1}$, significantly better than that of
116 undoped acid and structurally optimized control sample. A series of characterization results
117 indicate that the C=O group is the redox adsorption site for NH_4^+ , and microgravimetric
118 monitoring by an electrochemical quartz crystal microbalance with dissipation (EQCM-D)
119 further corroborates the reversibility of the ion adsorption/desorption process.

120

121 **2. Experimental methods**

122 *2.1. Material and chemicals*

123 1-Amino Anthraquinone (AAQ, $\geq 98\%$) were obtained from Shanghai Adamas Co., Ltd.



124 (Shanghai, China). Ammonium persulphate (APS, AR, $\geq 98\%$) was purchased from Shanghai
125 Titan Scientific Co., Ltd. (Shanghai, China). Acetonitrile (HPLC, 99.90 %) was obtained
126 from Shanghai Adamas Co., Ltd. (Shanghai, China). Perchloric acid (HClO_4 , GR, 70.0 –
127 72.0 %) was purchased from Yonghua Chemical Co., Ltd (Jiangsu, China). Ethanol absolute
128 (AR, $\geq 99.7\%$) was provided by Shanghai Lingfeng Chemical Reagents Co., Ltd. (China).

129 Activated carbon (AC) powder obtained from Shanghai Macklin Biochemical Co.Ltd.
130 (Shanghai, China). AC powder, carbon black (Shanghai Adamas Co., Ltd.) and
131 polyvinylidene fluoride (PVDF, Adamas, average $M_w \sim 534000$, RG) were combined at a
132 weight ratio of 8 : 1 : 1, followed by the addition of several drops of
133 1-Methyl-2-pyrrolidinone (NMP, $\geq 99.5\%$, Aladdin), and the mixture was stirred for more
134 than 12 h. This slurry was evenly coated onto a carbon paper and subsequently dried under
135 vacuum at $60\text{ }^\circ\text{C}$ to obtain an AC electrode with a thickness of approximately 0.1 mm.

136 2.2. Synthesis of PAAQ

137 Add 1.2780 g of APS to 20 mL of deionized water and sonicate to obtain a uniform APS
138 solution. Add 0.3125 g ($n_{\text{AAQ}} : n_{\text{APS}} = 1 : 4$) of AAQ monomer and 40 mL of acetonitrile to a
139 beaker, then drip 140 μL of HClO_4 and sonicate for 15 min to obtain a uniform orange yellow
140 transparent solution. The APS solution was then slowly added dropwise at a rate of one drop
141 every three seconds while the mixture was stirred at 300 rpm and maintained at $25\text{ }^\circ\text{C}$. The
142 color of the solution gradually turned dark orange, and stirring was continued at room
143 temperature for 48 h, resulting in the formation of a black precipitate. This solid product
144 (denoted as PAAQ-PS) was collected by centrifugation, washed sequentially with ethanol and
145 deionized water, and finally dried in a vacuum oven at $60\text{ }^\circ\text{C}$. In addition, two additional
146 samples were prepared under otherwise identical conditions to highlight the roles of acid and
147 stirring: PAAQ-S which involved stirring but no addition of protonic acid, and PAAQ-P
148 which involved the addition of protonic acid but no stirring during the dropwise addition and
149 subsequent reaction.

150 2.3. Material characterization

151 Scanning electron microscopy (SEM, GeminiSEM 300, Germany), X-ray diffractometer



152 (XRD, Rigaku Ultima IV, Japan), X-ray photoelectron spectroscopy (XPS, Thermo Scientific
153 K-Alpha, America), Fourier transform infrared spectrometer (FTIR, iS10, America),
154 Thermogravimetric analysis (TGA, TGA-1000C, China), Electrochemical workstation
155 (PGSTAT302N, Swiss), Electrochemical Quartz Crystal Microbalance with Dissipation
156 Monitoring (EQCM-D, Biolin, Swiss), Based on the N₂ adsorption/desorption isotherms
157 tested on Micromeritics ASAP 2460, the corresponding specific surface area (SSA) of the
158 different materials was calculated by Bruner Emmett Teller (BET). The pore size distributions
159 were calculated by Barret Joyner Halenda analysis (BJH).

160 2.4. Electrochemical measurements

161 The PAAQ material, CB, and PVDF were mixed at a mass ratio of 8:1:1 in NMP
162 solution and stirred for 24 hours to obtain a homogeneous slurry. The slurry was evenly
163 coated onto a carbon paper using a film applicator at a thickness of 1 μm. The coated area was
164 then carefully scraped to define a well-defined electrode region of 1 cm × 1 cm. After vacuum
165 drying at 60 °C to completely remove the solvent, the total mass of the dried active materials
166 on the electrode was approximately 0.5 mg. The resulting PAAQ electrode was then ready for
167 electrochemical tests.

168 Electrochemical tests were performed on a standard three-electrode system connected to
169 an electrochemical workstation. The as-synthesized PAAQ, a platinum sheet, and a saturated
170 Ag/AgCl electrode served as the working, counter, and reference electrodes, respectively.

171 The specific capacitance (C , F g⁻¹) was derived from the galvanostatic charge-discharge
172 (GCD) curves using the following equation:

$$173 \quad C = \frac{I \Delta t}{m \Delta V} (1)$$

174 Among them, I (A) is the discharging current, Δt (s) is the discharging duration, ΔV (V)
175 represents the voltage window, and m (g) refers to the mass of the active material on the
176 electrode.

177 Electrochemical-impedance spectroscopy (EIS) of the working electrode was recorded
178 on a workstation over the frequency window 0.01-10⁵ Hz. The spectra were analyzed and



179 fitted with equivalent circuits using ZView 3.3 software. The diffusion coefficient of NH_4^+ View Article Online
DOI: 10.1039/D6TA02416E
180 was subsequently extracted from the fitted data via the relationship⁴²:

$$181 \quad D_{\text{NH}_4^+} = \frac{R^2 T^2}{2A^2 n^4 F^4 C^2 \sigma^2} (2)$$

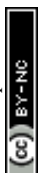
182 Among them, R refers to the gas constant, $8.314 \text{ J K}^{-1} \text{ mol}^{-1}$. T refers to the Kelvin
183 temperature. If tested at room temperature of $25 \text{ }^\circ\text{C}$, $T = 298.15 \text{ K}$. A refers to the area of the
184 electrode sheet, cm^2 . n refers to the number of electrons transferred during the reaction
185 process, 1. F refers to the faraday constant, 96485 C mol^{-1} . σ refers to the Warburg
186 coefficient, which is the slope of the line fitting Z' and $\omega^{-0.5}$. C refers to NH_4^+ concentration,
187 mol L^{-1} .

188

189 2.5. CDI experiment

190 The PAAQ electrode for CDI tests was prepared following the same coating and drying
191 procedure as described for the electrochemical tests, except that the coated region was $2 \text{ cm} \times$
192 2 cm and the dried active material mass was approximately 2 mg . The CDI cell was
193 assembled in a symmetric stack, comprising (from outside to center) fixed separators, gaskets,
194 conductive sheets, electrode materials, anion exchange membranes (AEM), chambers, cation
195 exchange membranes (CEM), and then the reverse order back to the outer fixed separators.
196 PAAQ and AC served as the cathode and anode materials, respectively. For each test, a 40
197 mL volume of 10 mM NH_4Cl solution was circulated through the system at a flow rate of 20
198 mL min^{-1} . Prior to applying voltage, the system was flushed with both deionized water and
199 the NH_4Cl solution to achieve physical adsorption equilibrium on the electrodes. The
200 concentration of NH_4Cl , which exhibits a linear relationship with solution conductivity, was
201 monitored indirectly by measuring conductivity every 10 seconds using a conductivity meter
202 (LeiCi, DDSJ-319L). All experiments were conducted in a sequential batch mode with
203 applied voltages ranging from 0.8 to 1.2 V .

204 The NH_4^+ removal behaviors of the CDI system were evaluated by NH_4^+ removal
205 capacity (NRC , mg g^{-1}) and NH_4^+ removal rate (NRR , $\text{mg g}^{-1} \text{ min}^{-1}$), which were



206 calculated according to the following equations:

$$207 \quad NRC = \frac{(C_0 - C_e) \times V}{m} \quad (3)$$

$$208 \quad NRR = \frac{NRC}{t} \quad (4)$$

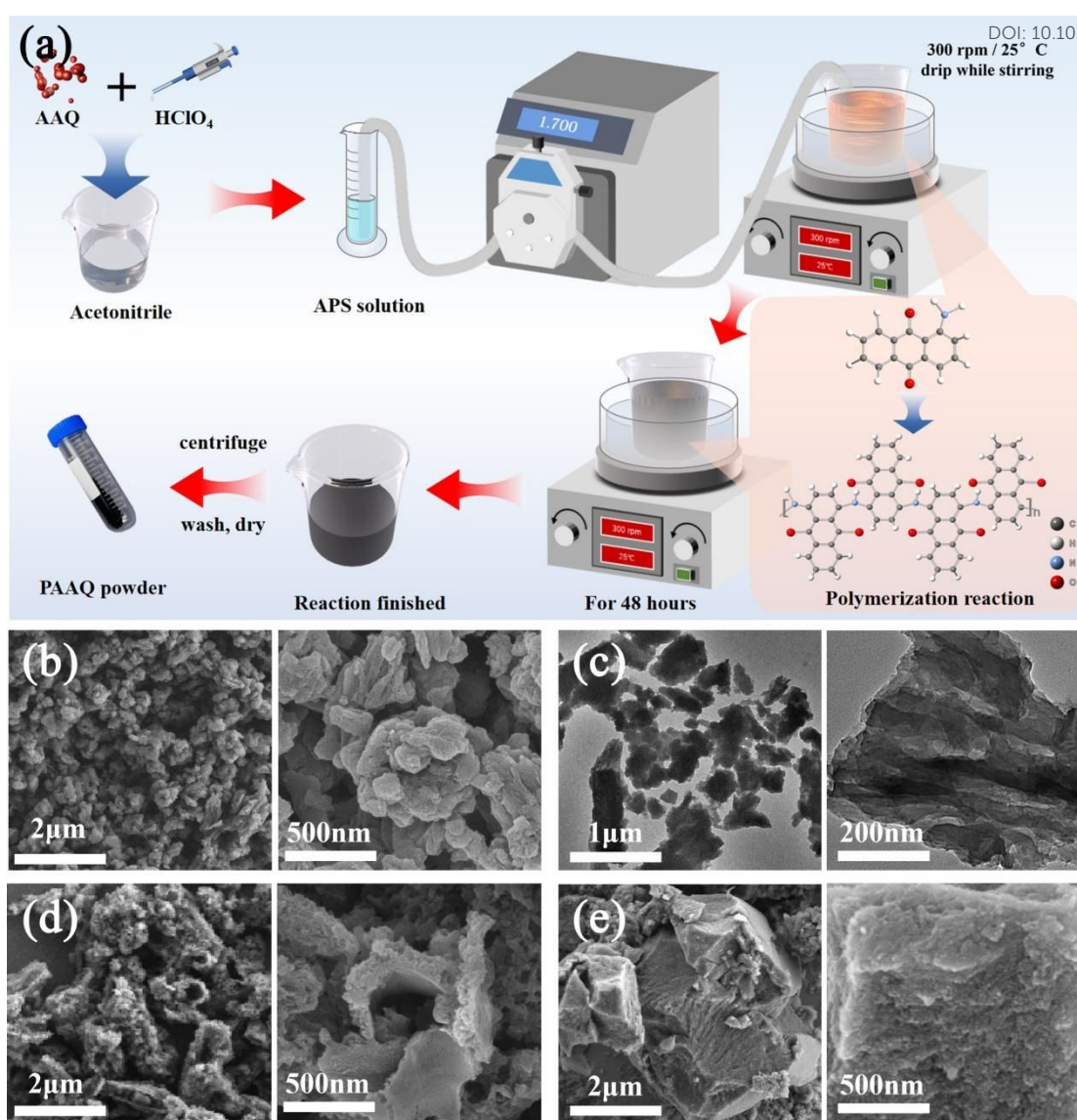
209 Where C_0 and C_e (mg L^{-1}) are the concentration of NH_4^+ at initial and final
210 stages, respectively; V (L) is the volume of NH_4Cl solution; m (g) represents
211 respective quality of electrode; t (min) refers to adsorption time.

212

213 3. Results and discussion

214 3.1. Synthesis and characterization of PAAQ

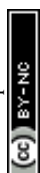




215

216 **Fig. 1.** Schematic diagram about the polymerization reaction of the PAAQ material (a), SEM (b) and
 217 TEM (c) images of PAAQ-PS, SEM images of PAAQ-S (d) and PAAQ-P (e).

218 The synthetic route to PAAQ is illustrated in Fig. 1a. AAQ monomers were initiated by
 219 protic acid (HClO₄) and propagated with APS as the oxidant, yielding PAAQ chains
 220 composed of -NH- linked repeat units. After 24 h of reaction, the initially dark-orange organic
 221 phase turned opaque-black, and a dense, black polymer film accumulated at organic-water
 222 interface. To drive the conversion to completion, the reaction was prolonged to 48 h, after
 223 which an abundant black precipitate had settled at the interface. The crude product was
 224 isolated by centrifugation and purified via successive washes with absolute ethanol (until the
 225 supernatant became colorless) to remove unreacted AAQ, followed by deionized water to



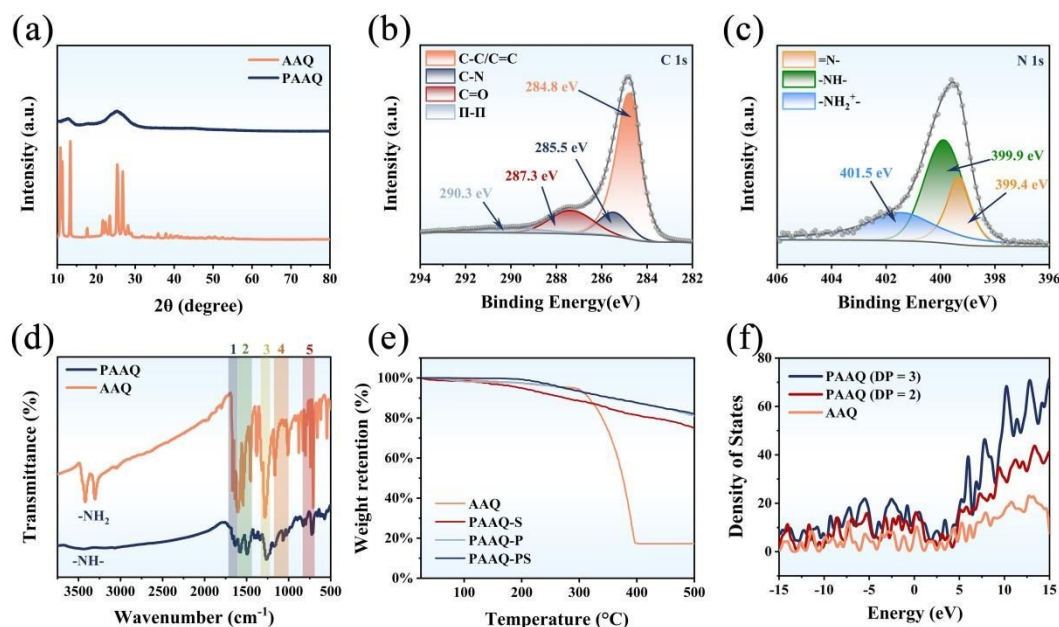
226 eliminate residual APS and neutralize residual acidity. The isolated PAAQ was obtained in
227 83.5 % isolated yield. SEM equipped with EDS was employed to investigate the sample's
228 morphology and elemental composition. As presented in Fig. S1, the EDS maps indicate a
229 homogeneous dispersion of C, N, and O across the analyzed area. To investigate the
230 promoting effect of protic acid and the structural tunability enabled by interfacial
231 polymerization, two control samples were prepared: (i) PAAQ-S (only stir), synthesized
232 under neutral conditions with stirring, and (ii) PAAQ-P (only protonic acid), prepared in the
233 presence of protic acid under static conditions. The sample prepared with simultaneous protic
234 acid addition and stirring is denoted as PAAQ-PS.

235 Vigorous stirring dispersed the aqueous APS solution into acetonitrile, generating
236 numerous nano-sized aqueous droplets that served as templates. At the resulting curved
237 oil-water interface, AAQ monomers from the organic phase underwent oxidative
238 polymerization, producing uniform polymer nanoparticles. As shown in the SEM image (Fig.
239 1b), the resulting PAAQ-PS material exhibits a well-dispersed, millet-like morphology. This
240 was further confirmed by TEM (Fig. 1c), which revealed alternating dark and light contrast
241 within individual grains, indicating thickness variations and confirming a three-dimensional
242 porous architecture with abundant voids. This internal porosity provides essential pathways
243 and a driving force for mass transport during the adsorption of water-based pollutants. In stark
244 contrast, when protic acid is omitted (PAAQ-S), polymerization is incomplete, affording
245 irregular, sub-nano fragments resembling the wreckage of a sphere (Fig. 1d). The necessity of
246 additional ethanol washes during purification corroborates the presence of substantial
247 unreacted monomer, resulting in a markedly lower isolated yield (53.1 %). It can therefore be
248 concluded that protic acids augment the involvement of monomeric species in the
249 polymerization reaction, thereby elevating the overall yield while simultaneously enforcing a
250 template-directed propagation that secures the as complete as possible growth of the polymer
251 along the template, ultimately affording control over the polymer's microscopic morphology.
252 Under static interfacial polymerization (PAAQ-P), the absence of mechanical agitation leads
253 to coalescence of the aqueous APS phase, producing a dense bulk (Fig. 1e) whose compact

View Article Online
DOI: 10.1039/D6TA02416E



254 architecture markedly differs from the small particulate morphology observed under stirred
 255 conditions. Such dense packing is anticipated to hinder active site accessibility, underscoring
 256 the influence of stirring on the microstructural evolution of interface-polymerization organic
 257 polymer.



258
 259 **Fig. 2.** (a) XRD patterns of PAAQ. High-resolution XPS spectra of (b) C 1s, (c) N 1s. (d) FTIR
 260 spectroscopy of AAQ and PAAQ. (e) TGA curve of samples. (f) the corresponding DOS for AAQ and
 261 PAAQ.

262 XRD patterns of the AAQ monomer and the corresponding polymer PAAQ are
 263 presented in Fig. 2a. The monomer exhibits a series of intense, well-defined Bragg reflections
 264 indicative of its high crystallinity. Upon oxidative polymerization, these sharp peaks collapse
 265 into broad, low-intensity humps centered at $2\theta = 25^\circ$, which is the signature of π - π stacking
 266 between polymer backplanes^{35, 43}. XPS analysis revealed the elemental composition and
 267 bonding states of PAAQ. High-resolution C 1s spectrum can be deconvoluted into four peaks
 268 centered at 284.8, 285.7, 287.5 and 290.3 eV, assigned to C-C/C=C, C-N, C=O and π - π
 269 stacking, respectively (Fig. 2b). Similarly, the N 1s spectrum (Fig. 2c) could be deconvoluted
 270 into three peaks at 399.4, 399.9 and 401.5 eV, corresponding to the quinonoid imine (=N-),
 271 amine (-NH-), and positively charged nitrogen (N⁺) species^{44, 45}. The presence of the =N-
 272 component evidences an extended π -conjugation pathway between the lone pair on nitrogen
 273 and the anthraquinone π -system⁴⁶, facilitating delocalization of charge carriers across the



274 polymer backbone and imparting superior electron-transport characteristics. The sole O 1s
275 component at 532.4 eV (Fig. S2) is ascribed to carbonyl oxygen (C=O) within the quinonoid
276 rings.

277 FTIR spectra of AAQ and PAAQ are displayed in Fig. 2d. For the monomer, the
278 symmetric and asymmetric N–H stretching vibrations of the terminal –NH₂ group are
279 observed at 3420 and 3300 cm⁻¹, respectively⁴⁷. After oxidative polymerization, these two
280 peaks coalesce into a single broad envelope centered at 3470 cm⁻¹, confirming the conversion
281 of –NH₂ into –NH– group within the polymer backbone⁴⁸. Additional spectral signatures can be
282 summarized as follows: (1) A strong band at 1640 cm⁻¹, common to both AAQ and PAAQ, is
283 ascribed to the C=O stretching vibration of the quinonoid carbonyl. (2) PAAQ exhibits two
284 well-resolved peaks at 1580 cm⁻¹ and 1490 cm⁻¹ that are attributed to in-plane skeletal
285 vibrations of the quinonoid and benzenoid rings, respectively. In contrast, AAQ displays three
286 broader and less-defined bands in the same region, reflecting the shorter effective conjugation
287 length of the monomer⁴⁹. (3) The aromatic C–N stretching mode at 1290 cm⁻¹ in AAQ
288 undergoes a red-shift to 1270 cm⁻¹ in PAAQ, consistent with the formation of C–NH–C
289 bridges upon polymerization^{50, 51}. (4) The series of bands between 1180 to 1010 cm⁻¹ originate
290 from in-plane C–H deformation modes. (5) Out-of-plane bending vibrations appear at 827 and
291 800 cm⁻¹ (two adjacent C–H) and 723 and 710 cm⁻¹ (three adjacent C–H) on the benzene ring.
292 FTIR spectra of the control samples (Fig. S3) demonstrate that PAAQ-S retains most of the
293 characteristic peaks of AAQ, including the free –NH₂ stretches, corroborating the incomplete
294 polymerization in the absence of protic acid. Conversely, PAAQ-P exhibits spectral features
295 nearly identical to those of PAAQ, indicating that mechanical stirring influences
296 microstructure rather than the intrinsic chemical functionality of the polymer.

297 TGA demonstrates a pronounced improvement in thermal stability upon polymerization
298 (Fig. 2e). PAAQ exhibits negligible mass loss below 200 °C and retains >90 % weight
299 retention at 300 °C. The subsequent degradation is also very slow, and PAAQ-S may exhibit
300 slightly weaker thermal stability than the other two polymerization products due to
301 incomplete polymerization. In stark contrast, the AAQ monomer undergoes catastrophic



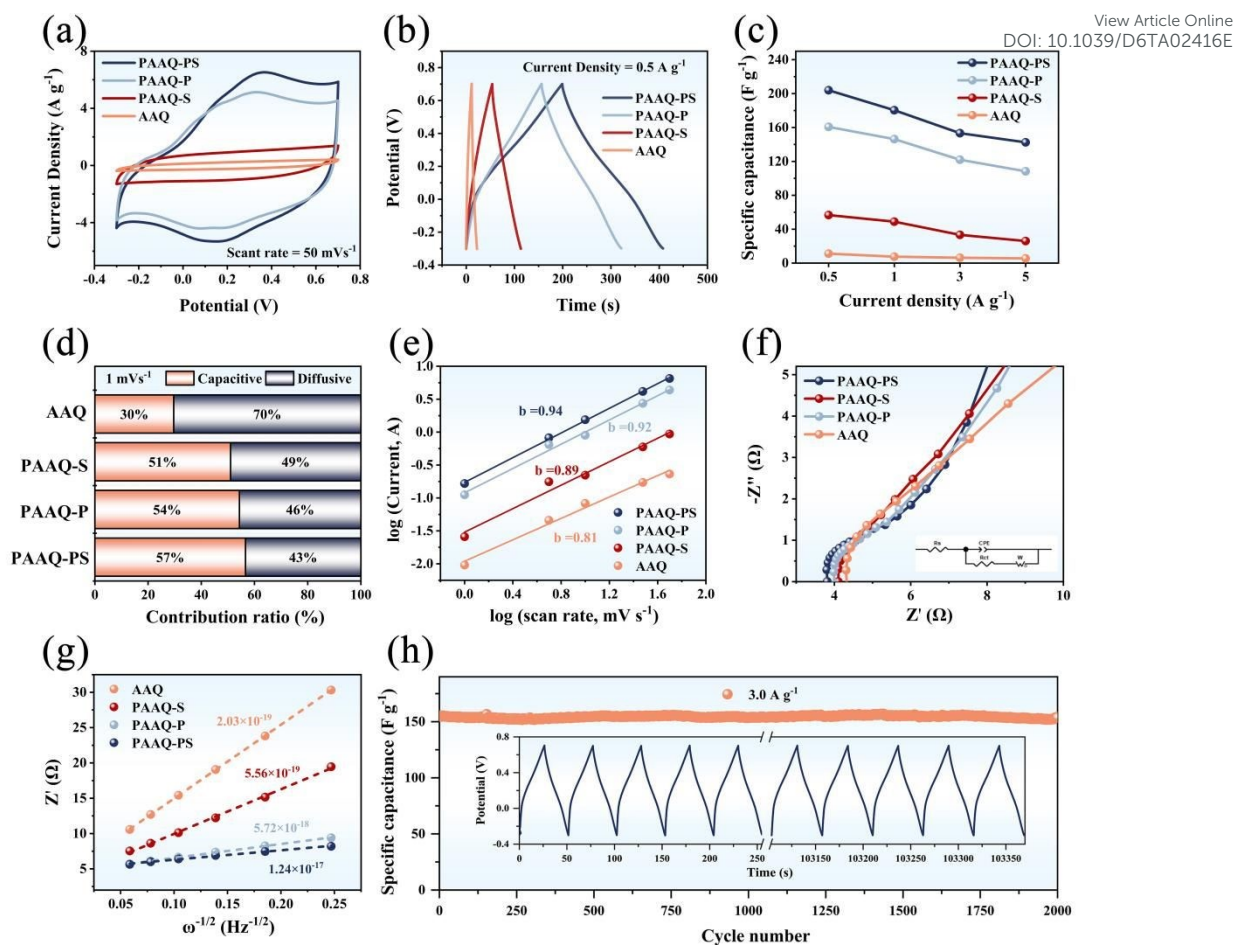
302 decomposition above 300 °C, retaining merely 20 % of its initial mass at 400 °C. These
303 results attesting to the robustness of the polymer backbone. Variations in the density-of-states
304 (DOS) at the Fermi level occurring in the pores of AAQ and PAAQ (polymerization degree =
305 2, 3) were further investigated by using VASP AIMD simulations (Fig. 2f). The results
306 indicate that the formation of a more complete π -conjugated framework through further
307 polymerization reaction may enhance the density of states on the material surface, which is
308 expected to promote the transfer of electrons on the polymer chain and enhance the overall
309 conductivity of the material⁵². N₂ sorption isotherms and pore-size distributions of the four
310 samples are presented in Fig. S5. According to the IUPAC classification⁵³, both PAAQ and
311 PAAQ-P exhibit Type IV isotherms (Fig. S4a). A gradual uptake at low-to-intermediate
312 relative pressures ($p/p_0 < 0.4$) indicates a lack of micropores structure, whereas a pronounced
313 capillary condensation step accompanied by a clear H₃-type hysteresis loop at $p/p_0 > 0.8$ is
314 diagnostic of a mesopore/macropore network. This feature is more pronounced for PAAQ-P.
315 The corresponding BJH pore-size distributions (Fig. S4b) corroborate the predominance of
316 mesopores (2-50 nm) and macropores (> 50 nm) in all polymerized products. BET analysis
317 yields the following SSA: PAAQ-S (27.59 m² g⁻¹) > PAAQ-PS (19.53 m² g⁻¹) > PAAQ-P
318 (15.35 m² g⁻¹) > AAQ (2.67 m² g⁻¹). For applications of electrode materials, higher SSA
319 shortens ion-diffusion pathways, enhances charge-storage capacity and improves adsorption
320 kinetics. Notably, all polymeric products possess markedly larger SSAs than the AAQ
321 monomer, ensuring abundant electroactive sites. The exceptionally high SSA of PAAQ-S
322 originates from its fragmented, incompletely polymerization morpholog. But this
323 morphological characteristic does not necessarily translate to superior electrosorption
324 performance. Conversely, the quiescent interfacial polymerization of PAAQ-P yields a
325 compact, agglomerated architecture, resulting in the lowest SSA among the polymers.

326

327 *3.2. Electrochemical characterization*

View Article Online
DOI: 10.1039/D6TA02416E





328

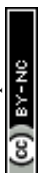
329 **Fig. 3.** (a) CV and (b) GCD curves of various organic electrodes in 1 M NH₄Cl solution. (c) GCD
 330 specific capacitances, (d) contribution of capacitance and diffusion control capacity, (e) power-law
 331 relationship between oxidation peak current and scan rate of organic electrodes. (f) Nyquist plot of
 332 organic electrodes and equivalent circuit diagram. (g) NH₄⁺ diffusion coefficient of organic electrodes.
 333 (h) Long-term cycling performance and corresponding GCD curves of the PAAQ electrode at 3 A g⁻¹.

334 The various organic electrodes was characterized by conventional three-electrode
 335 configuration (Fig. S5-8). Cyclic voltammetry (CV) and galvanostatic charge-discharge
 336 (GCD) curves (Fig. 3a-b) reveal a quasi-reversible redox couple for both PAAQ-PS and
 337 PAAQ-P, which can be attributed to the enolization of C=O to C-OH on the anthraquinone
 338 core^{54, 55}. This transformation confirms that PAAQ possesses redox-active sites capable of
 339 NH₄⁺ storage. Notably, the redox peak is close to zero potential, indicating facile activation of
 340 these sites⁵⁶. In contrast, both PAAQ-S and AAQ exhibit almost pure electrical double layer
 341 behavior at higher scanning rates, with only weak and far from zero potential redox signals
 342 observed at scanning rates below 10 mV s⁻¹ (Fig. S7f) and 1 mV s⁻¹ (Fig. S8h) respectively.



343 These observations corroborate that C=O on the conjugated backbone are intrinsically
344 redox-active. P-doping of PAAQ chain owing to the protonation of -NH-, triggers an
345 extensive delocalization of the π -electron cloud across the anthraquinone scaffold, thereby
346 expanding the π -conjugated structure and markedly optimizing energy bandgap and electronic
347 properties^{57, 58}. Consequently, the redox-active sites are electronically activated⁵⁹, manifesting
348 as a pronounced decrease in the redox potential and substantial increase in integrated peak
349 area. Although PAAQ-S bears a comparatively weak π -system, its CV and GCD curves
350 display lower polarization than those of monomeric AAQ (Fig. S7a-b, Fig. S8a-b),
351 underscoring low degree of π -conjugated can still provide minor additional capacitance
352 performance. As shown in Fig. 3c, the specific capacitance of different electrode materials
353 measured at 0.5 A g⁻¹ in the order : PAAQ-PS (203.95 F g⁻¹) > PAAQ-P (160.73 F g⁻¹) >
354 PAAQ-S (56.65 F g⁻¹) > AAQ (11.2 F g⁻¹). The superior performance of PAAQ-PS relative to
355 PAAQ-P stems from stirring operation during the polymerization process, which possibly
356 suppresses excessive π - π stacking of the polymer chains under static conditions, optimizing
357 charge distribution and extending further electron delocalization⁵⁶. In contrast, the
358 pronounced advantage of PAAQ-PS over both PAAQ-S and AAQ originates from the
359 post-protonation expansion of π -conjugation, which simultaneously unlocks latent redox
360 activity and cooperatively amplifies ion-storage capacity. Overall, the above results
361 demonstrate that the strategy of protonation to regulate electron delocalization possibly exert
362 a more decisive influence on capacitance of PAAQ than do structural modifications.

363 To gain deeper insight into the capacitive response of organic electrode materials, the
364 fraction of diffusion-controlled capacitance was quantified (Fig. 3d). The theory proposed by
365 Duun et al can quantitatively calculate the ratio of current generated by diffusion control and
366 capacitance control at a certain scanning rate: $i = k_1v + k_2v^{0.560}$, k_1v and $k_2v^{0.5}$ represent surface
367 capacitance control current and diffusion control current, respectively. Owing to the rapid
368 surface-capacitive kinetics imparted by the wider range of electron delocalized π -conjugated
369 skeleton, the quinone-based electrodes in this work exhibit a markedly higher capacitive
370 contribution than most previously documented organic or ammonium-selective electrodes^{30, 34}.



371 ^{54, 61, 62}. At the scan rate of 1 mV s⁻¹, the capacitive ratios are 30 % for AAQ, 51 % for
372 PAAQ-S, 54 % for PAAQ-P, and 57 % for PAAQ-PS. These imply that proportion of
373 capacitance control is possibly governed predominantly by the extended π -conjugated which
374 emerges after polymerization, whereas redox sites exert secondary influence. Among these,
375 PAAQ-PS presents the largest capacitive proportion, indicating its superior applicability for
376 rapid storage of NH₄⁺. A power-law analysis correlating the current response with scan rate
377 was performed based on the CV results. Typically, dynamics of electrode are divided into
378 capacitance control and diffusion control. The scan rate (ν) versus current (i) relationship
379 follows a power-law dependence, $i = a\nu^b$, where a and b are adjustable parameters obtained
380 from the linear fitting of $\log i$ versus $\log \nu$. The b -value of 0.5 indicates that
381 diffusion-controlled reactions dominate, while a b -value of 1.0 indicates complete capacitive
382 behavior⁶³. The b -values of four organic materials were obtained by calculating the currents
383 of the oxidation peak and reduction peak at different scan rate (Fig. S5-8i). Notably, certain
384 difference in b -values is observed between PAAQ-PS and PAAQ-P, while PAAQ-S and AAQ
385 have almost no such phenomenon, especially AAQ. Combined with slight asymmetry of the
386 CV curves, this indicates that the additional enolization mechanism does not conform to a
387 simple reversible kinetic relationship possibly. Fig. 3e presents the b -values derived from the
388 anodic peak currents of all four materials. Approaching 1.0 for the three polymer electrodes'
389 b -values signify that dynamics is governed predominantly by capacitive processes,
390 corroborating the quantitative capacitive-diffusion contribution analysis.

391 Electrochemical impedance spectroscopy (EIS) measurements yielded the Nyquist plot
392 presented in Fig. 3f. The high-frequency intercept and semicircle diameter represent the
393 solution resistance (R_s) and charge-transfer resistance (R_{ct}), respectively. Fitted values follow
394 the sequence R_s : PAAQ-PS (3.81 Ω) < PAAQ-P (4.01 Ω) < PAAQ-S (4.10 Ω) < AAQ (4.33
395 Ω); R_{ct} : PAAQ-PS (3.14 Ω) < PAAQ-P (5.85 Ω) < PAAQ-S (6.88 Ω) < AAQ (15.49 Ω). The
396 exceptionally low R_s and R_{ct} of PAAQ-PS are ascribed to the electron delocalization of its
397 polymer chains and optimized surface-charge distribution in a rice-grain morphology, which
398 facilitate rapid electron/ion transport and enhance redox kinetics³⁵. The Warburg coefficient

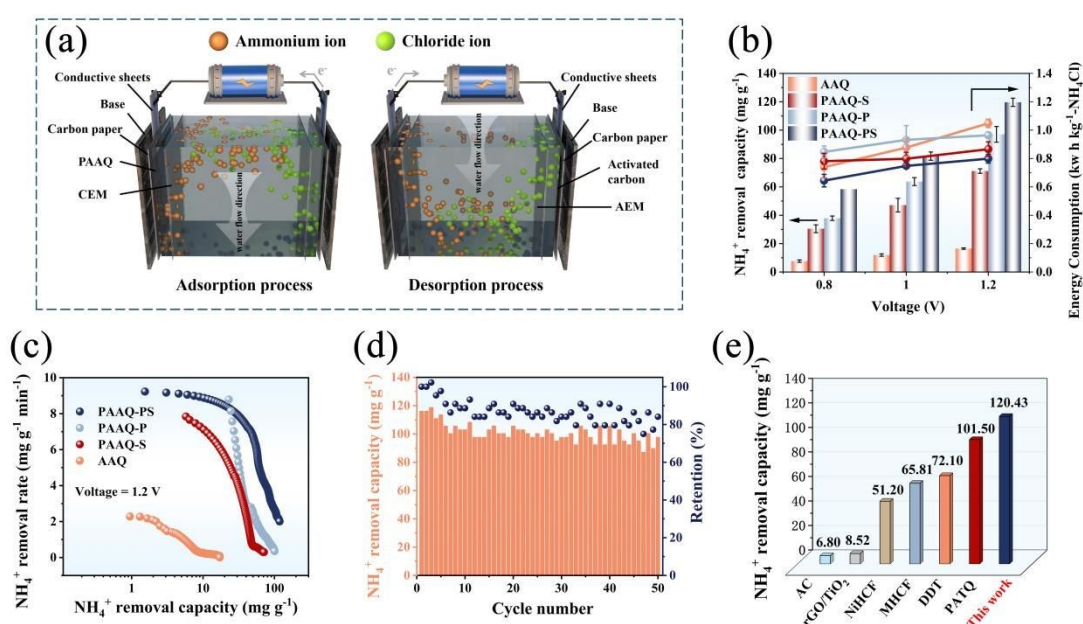


399 (Rw), derived from the low-frequency linear region, decreases in the order PAAQ-PS ^{View Article Online}
 DOI: 10.1039/D6TA02416E
 400 PAAQ-P < PAAQ-S < AAQ, corroborating the smallest Rw for PAAQ-PS⁶⁴. Consequently,
 401 based on Eq. (2), the NH₄⁺ diffusion coefficient (Fig. 3g) is highest for PAAQ-PS (1.2 ×
 402 10⁻¹⁷), affirming its superior pseudocapacitive behavior. Cyclic stability was evaluated by
 403 GCD cycling at 3.0 A g⁻¹. Over 2000 cycles, PAAQ-PS exhibited negligible capacitance fade
 404 (Fig. 3h), underscoring its outstanding electrochemical reversibility. Organic
 405 pseudocapacitive materials robustness is attributed to its reliance on functional groups as
 406 redox-active sites for ion adsorption, in contrast to storage mechanisms involving phase
 407 transitions. This property enables it to circumvent issues like the substantial volume
 408 expansion observed in many inorganic materials, while preserving excellent structural
 409 integrity throughout extended cycling..

410

411

3.3. CDI performance evaluation



412

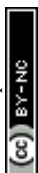
413 **Fig. 4.** (a) Schematic of the PAAQ//AC HCDI process. NH₄⁺ removal capacity, energy consumption(b)
 414 and Ragone plots (c) of PAAQ under various voltages. (d) Cycling performances and retention values
 415 of PAAQ electrodes at 1.2V. (e) NH₄⁺ removal capacity comparison of other electrode materials.

416 To evaluate the efficiency of the HCDI system for NH₄⁺ removal, adsorption
 417 experiments were conducted by using a custom-built CDI device. As showed in Fig.4a, the



418 device was configured with PAAQ electrode material as the cathode for adsorbing NH_4^+ and
419 commercially available activated carbon as the anode for adsorbing Cl^- . Upon reversing the
420 voltage, the ions adsorbed on the electrode were desorbed, and the electrode achieves
421 regeneration. To prevent the capture of ions during voltage reversal, an anion exchange
422 membrane (AEM) and a cation exchange membrane (CEM) were positioned adjacent to the
423 anode and cathode surfaces, respectively. During the process of increasing the applied voltage
424 from 0.8 V to 1.2 V, the specific adsorption capacity of organic electrodes for NH_4^+
425 significantly increased, indicating that high voltage helps enhance the deionization ability of
426 HCDI devices (Fig. 4b). Adsorption capacities toward NH_4^+ at 1.2 V were calculated by Eq.
427 (3) and followed the order: PAAQ-PS (120.43 mg g^{-1}) > PAAQ-P (100.52 mg g^{-1}) > PAAQ-S
428 (70.83 mg g^{-1}) > AAQ (17.13 mg g^{-1}) (Fig. 4b), a trend that mirrors the preceding
429 electrochemical metrics. The highest specific capacitance observed for PAAQ-PS translates
430 into the best NRC. The Ragone plot (Fig. 4c) shows that the PAAQ-PS electrode shifts
431 furthest toward the upper-right quadrant, evidencing simultaneously elevated NRC and NRR.
432 A high NRR of $9.23 \text{ mg g}^{-1} \text{ min}^{-1}$ was achieved by the HCDI device during the initial
433 adsorption phase under 1.2 V operation. Attributed to its rapid surface redox reaction, the
434 performance surpasses that of polymers obtained through previous synthetic methods of
435 AAQ⁵⁵. Combined with the result of electrochemical test, the adsorption performance gain is
436 ascribed the global upshift in electronic conductivity coupled with judicious microstructure
437 optimization, highlighting the advantages of the protonation regulation and interfacial
438 polymerization approach.

439 Conversely, the bulky morphology of PAAQ-P induces steric shielding of redox-active
440 moieties and excessive π - π stacking, both of which impede interfacial charge transfer and
441 yield a marginally lower NRC than the rice-shaped PAAQ-PS. These observations underscore
442 the potential of morphology engineering for low-crystallinity organic frameworks whose
443 architectures are highly tunable. PAAQ-S suffers from a poor-continuity π -conjugated
444 network due to lack of Polarization induced electron delocalization. Although it possesses the
445 highest SSA, restricted electron mobility prevents full activation of surface redox sites,

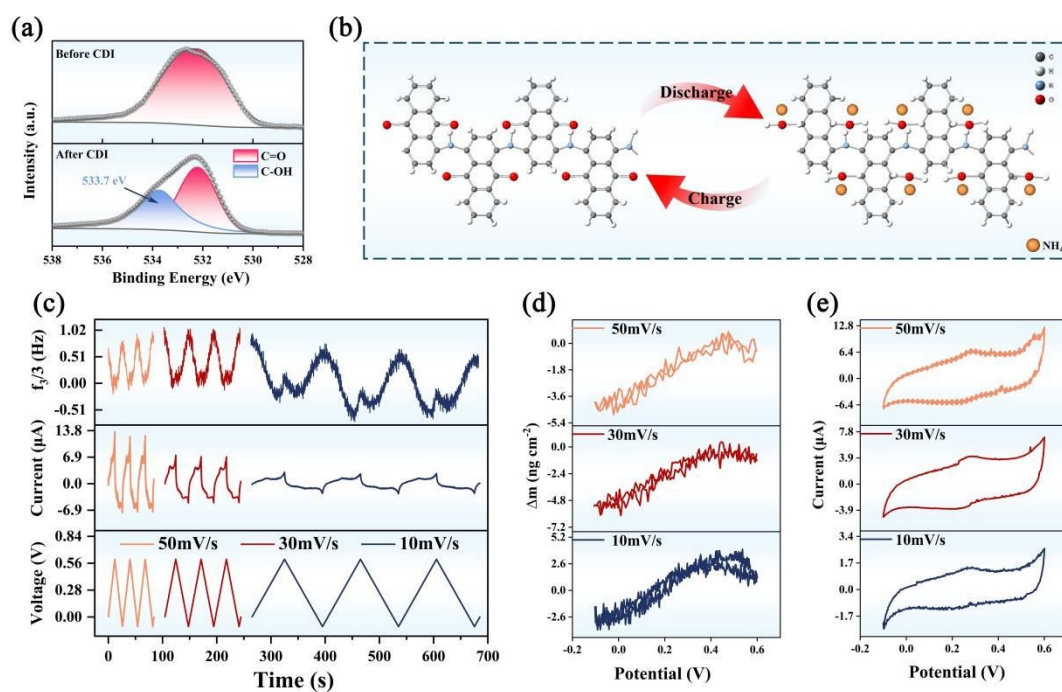


446 thereby diminishing NH_4^+ adsorption. Nevertheless, its capacity still exceeds that of pristine
 447 AAQ, confirming that the partially conjugated segments generated by moderate
 448 polymerization do facilitate electron transport. Relative to PAAQ synthesized under acidic
 449 conditions, however, a pronounced performance gap persists, highlighting the pivotal role of a
 450 well-developed π -conjugated framework in achieving superior NH_4^+ capture. A critical factor
 451 in judging CDI electrode performance is their long-term stability. To determine the
 452 reversibility and cyclic stability of PAAQ electrodes within a CDI device, cycling
 453 performance was assessed in a 1.2 V NH_4Cl solution (Fig. 4d). After 50 cycles, the NRC of
 454 PAAQ-PS was maintained at 84.1% of its initial value, confirming its satisfactory cyclic
 455 stability. Compared to previous ammonium removal electrode materials, PAAQ-PS exhibits
 456 both good adsorption capacity (Fig. 4e)^{23, 24, 54, 55, 65, 66}.

457

458

3.4. Ionic deintercalation mechanism



459

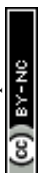
460 **Fig. 5.** (a) High-resolution XPS spectra of O 1s for PAAQ before and after CDI. (b) Structural
 461 evolutions of PAAQ upon enolization for NH_4^+ uptake/removal. (c) Time-dependent changes in $\Delta f_3/3$,
 462 current and voltage of PAAQ at different scan rates measured via EQCM. The corresponding mass
 463 change (d) and current change (e) of PAAQ at various scan rates.

464 To elucidate the NH_4^+ storage mechanism of PAAQ, ex-situ XPS was performed on the



465 PAAQ-PS electrode before and after CDI (Fig. 5a). The O 1s spectra reveal that only a C=O
466 component at 532.4 eV is present prior to CDI. After NH_4^+ uptake, the C=O peak attenuates
467 concomitantly with the emergence of a new C-OH feature at 533.7 eV. This spectral evolution
468 corroborates the enolization of quinonyl C=O moieties to C-OH, thereby enabling reversible
469 NH_4^+ storage (Fig. 5b), in agreement with prior studies^{54, 55}. Specifically, a negative voltage is
470 applied to the PAAQ electrode during the CDI adsorption step. The C=O on the PAAQ
471 backbone are reduced to C-OH. This reduction imparts a stronger electronegativity to the
472 oxygen atom, enabling it to bind NH_4^+ through hydrogen bonding or chelation, thereby
473 forming a C-OH- NH_4^+ structure. This additional binding mode increases the upper limit of
474 NH_4^+ adsorption. When the voltage is inverted, the C-OH groups are oxidized back to C=O.
475 This transformation weakens the affinity for NH_4^+ , and together with the electrostatic
476 repulsion from the positive potential, NH_4^+ is efficiently released from the electrode. The
477 electrodes of PAAQ-P, PAAQ-S, and AAQ after CDI were further tested by XPS (Fig. S9).
478 Only PAAQ-P mirrors the behavior of PAAQ-PS, exhibiting a pronounced enolization
479 signature through the appearance of C-OH functionalities alongside attenuated C=O signals.
480 In contrast, PAAQ-S and AAQ retain their original C=O profiles after CDI, owing to their
481 incomplete π -conjugation, which precludes activation of the quinone redox centers. This
482 spectroscopic evidence is consistent with the electrochemical results.

483 To further quantify ionic fluxes during adsorption/desorption, EQCM-D was coupled to
484 cyclic voltammetry. Fig. 5c shows that, during the anodic sweep at progressively lower scan
485 rates, the normalized frequency shift ($\Delta f_3/3$) decreases stepwise, signifying Cl^- adsorption and
486 a concomitant increase in PAAQ mass. Upon cathodic polarization, Cl^- is expelled while
487 NH_4^+ is incorporated. The overall mass declines because the molar mass of desorbed Cl^-
488 exceeds that of adsorbed NH_4^+ . Notably, the transition from anodic to cathodic polarization
489 induces a transient frequency reversal: the mass initially rises slightly before monotonically
490 decreasing. This effect intensifies at slower scan rates, suggesting a diffusion-limited
491 enolization of residual C=O groups that facilitates additional NH_4^+ uptake, potentially
492 exceeding the mass loss from Cl^- release. The closed Δm -potential hysteresis loop in Fig. 5d



493 demonstrates the robust cyclability of PAAQ under repeated redox behavior. Although the net
494 mass loss per cycle is negligible, it is evident that as the scan rate decreases, the magnitude of
495 mass change within a single cycle increases significantly. This observation indicates that at
496 lower scan rates, ions have sufficient time to diffuse fully into the interior of the electrode
497 material, thereby enabling more pronounced mass variation. Moreover, the lower scan rate
498 accentuates the mass reversal phenomenon, that is, the transient frequency reversal around the
499 potential switching point, further demonstrating that the enolization-driven pseudocapacitive
500 effect is more fully realized under slower kinetic conditions.

501 Fig. 5e displays the CV recorded simultaneously with the EQCM-D measurements.
502 Although a well-defined redox couple is still discernible, its formal potentials are displaced
503 further from zero potential point relative to those observed in conventional CV performed on
504 coated electrodes. This shift may be ascribed to the higher degree of dispersion of the
505 electroactive film on the quartz-crystal chip, which disrupts the π - π stacking that normally
506 endows conjugated polymers with their certain electrochemical characteristics⁵⁶. Taking the
507 scan rate of 10 mV s⁻¹ as representative, the potential at which the mass transition changes
508 from an initial increase to a subsequent decrease, as illustrated in Fig. 5d, coincides almost
509 exactly with the cathodic peak potential in the CV. This correspondence demonstrates that,
510 once the applied potential falls below this value, enolization-driven NH₄⁺ uptake by PAAQ
511 ceases. Consequently, the expulsion of Cl⁻ and the sorption of NH₄⁺ reach a dynamic
512 equivalence in molar terms, manifesting as a net decrease in the overall electrode mass.

513

514 4. Conclusion

515 In summary, this work successfully prepared PAAQ nanomaterials with abundant redox
516 active sites and appreciable electronic conductivity through a mild strategy combining
517 protonation and interfacial polymerization. This method effectively solved the problem of
518 insufficient active sites and slow adsorption rate caused by diffusion control in traditional
519 organic materials. PAAQ-PS demonstrates significantly enhanced NH₄⁺ adsorption



520 performance over both the non-acid-mediated PAAQ-S and the statically polymerized
521 PAAQ-P. This advantage arises from its combination of improved conductivity, due to
522 electron delocalization from -NH_2^+ polarons, and a morphology that facilitates the exposure
523 of redox-active sites. The experimental results showed that under voltage of 1.2 V, the
524 adsorption capacity of PAAQ for NH_4^+ reached 120.43 mg g^{-1} , with an adsorption rate of 9.22
525 $\text{mg g}^{-1} \text{ min}^{-1}$, and it could still maintain 84.1% of the initial adsorption capacity after 50
526 cycles, demonstrating excellent cycling stability and rapid adsorption ability. This study
527 provides innovative ideas for activate the redox active sites of organic conjugated polymers to
528 enhance their adsorption capacity, further promoting the application and development of CDI
529 technology in the fields of NH_4^+ removal and resource recovery.

530

531 **Acknowledgment**

532 This research is supported by The National Natural Science Foundation of China
533 (22276137, 22576153), Tianshan Innovation Team of Xinjiang Uygur Autonomous
534 Region(2025D14023), and Outstanding Youth Science Fund Project of Xinjiang
535 Uygur Autonomous Region(2025D01E22). This work was funded by Xinjiang
536 Leading Talent Program (XJRC-2025-KJ-YJ-CXPT-214) and the Xinjiang Key
537 Laboratory of Engineering Materials and Structural Safety Open Science Project
538 (XKLEMSS2025B07).

539

540 **Reference**

- 541 1 Q. C. Xu, S. X. Wang, J. K. Jiang, N. Bhattarai, X. X. Li, X. Chang, X. H. Qiu, M.
542 Zheng, Y. Hua and J. M. Hao, Nitrate dominates the chemical composition of $\text{PM}_{2.5}$
543 during haze event in Beijing, China, *Sci. Total Environ.*, 2019, 689, 1293-1303.
- 544 2 Z. P. Zhao, B. Wang, Q. W. Feng, M. Chen, X. Y. Zhang and R. H. Zhao, Recovery
545 of nitrogen and phosphorus in wastewater by red mud-modified biochar and its
546 potential application, *Sci. Total Environ.*, 2023, 860, 15.
- 547 3 J. K. Song, X. Zhao, R. R. Liu, Y. H. Wang, D. Y. Zhu, X. Y. Wang, K. Jiang and D.
548 P. Wu, Simultaneous removal and recovery of ammonium and phosphate ions using
549 flow electrode capacitive deionization through the struvite generation mechanism,
550 *Sep. Purif. Technol.*, 2025, 358, 11.



- 551 4 T. Cai, D. Zhao and E. Gutmark, Overview of fundamental kinetic mechanisms and
552 emission mitigation in ammonia combustion, *Chem. Eng. J.*, 2023, 458, 17. View Article Online
DOI: 10.1039/D6TA02416E
- 553 5 M. Van Damme, L. Clarisse, S. Whitburn, J. Hadji-Lazaro, D. Hurtmans, C. Clerbaux
554 and P. F. Coheur, Industrial and agricultural ammonia point sources exposed, *Nature*,
555 2018, 564, 99-+.
- 556 6 Q. Q. Yin, R. K. Wang and Z. H. Zhao, Application of Mg-Al-modified biochar for
557 simultaneous removal of ammonium, nitrate, and phosphate from eutrophic water, *J.*
558 *Clean Prod.*, 2018, 176, 230-240.
- 559 7 P. M. Glibert, F. P. Wilkerson, R. C. Dugdale, J. A. Raven, C. L. Dupont, P. R.
560 Leavitt, A. E. Parker, J. M. Burkholder and T. M. Kana, Pluses and minuses of
561 ammonium and nitrate uptake and assimilation by phytoplankton and implications for
562 productivity and community composition, with emphasis on nitrogen-enriched
563 conditions, *Limnol. Oceanogr.*, 2016, 61, 165-197.
- 564 8 Y. M. Yang, B. B. Tao, C. H. Liu, M. H. Li, W. J. Wu, Y. Y. She, J. Zhang, H. K.
565 Thabet, M. H. Helal, Z. M. El-Bahy and X. T. Xu, Capacitive deionization for
566 ammonia recovery: Progresses and challenges, *Chem. Eng. J.*, 2024, 500, 21.
- 567 9 P. P. Li, Z. Y. Jin, Z. W. Fang and G. H. Yu, A single-site iron catalyst with
568 preoccupied active centers that achieves selective ammonia electrosynthesis from
569 nitrate, *Energy Environ. Sci.*, 2021, 14, 3522-3531.
- 570 10 J. Choi, B. H. R. Suryanto, D. B. Wang, H. L. Du, R. Y. Hodgetts, F. M. F. Vallana,
571 D. R. MacFarlane and A. N. Simonov, Identification and elimination of false
572 positives in electrochemical nitrogen reduction studies, *Nat. Commun.*, 2020, 11, 10.
- 573 11 A. Valera-Medina, F. Amer-Hatem, A. K. Azad, I. C. Dedoussi, M. de Joannon, R. X.
574 Fernandes, P. Glarborg, H. Hashemi, X. He, S. Mashruk, J. McGowan, C.
575 Mounaim-Rouselle, A. Ortiz-Prado, A. Ortiz-Valera, I. Rossetti, B. Shu, M. Yehia, H.
576 Xiao and M. Costa, Review on Ammonia as a Potential Fuel: From Synthesis to
577 Economics, *Energy Fuels*, 2021, 35, 6964-7029.
- 578 12 H. Cruz, Y. Y. Law, J. S. Gues, K. Rabaey, D. Batstone, B. Laycock, W. Verstraete
579 and I. Pikaar, Mainstream Ammonium Recovery to Advance Sustainable Urban
580 Wastewater Management, *Environ. Sci. Technol.*, 2019, 53, 11066-11079.
- 581 13 M. R. Adam, M. H. D. Othman, R. Abu Samah, M. H. Puteh, A. F. Ismail, A.
582 Mustafa, M. A. Rahman and J. Jaafar, Current trends and future prospects of
583 ammonia removal in wastewater: A comprehensive review on adsorptive membrane
584 development, *Sep. Purif. Technol.*, 2019, 213, 114-132.
- 585 14 M. S. Miah, N. Amjady, R. Shah and S. Islam, Energy Recovery From Polluted
586 Water Using Capacitive Deionization Desalination System: A Review, *IEEE Access*,
587 2024, 12, 110002-110027.
- 588 15 M. J. Liu, M. Y. He, J. L. Han, Y. Y. Sun, H. Jiang, Z. Li, Y. N. Li and H. F. Zhang,
589 Recent Advances in Capacitive Deionization: Research Progress and Application
590 Prospects, *Sustainability*, 2022, 14, 41.
- 591 16 J. Ma, R. H. Zhou and F. Yu, Hotspots and future trends of capacitive deionization
592 technology: A bibliometric review, *Desalination*, 2024, 571, 11.
- 593 17 J. Ma, C. X. Zhai and F. Yu, Review of flow electrode capacitive deionization
594 technology: Research progress and future challenges, *Desalination*, 2023, 564, 21.



- 595 18 N. L. Liu, S. H. Sun and C. H. Hou, Studying the electrosorption performance of
596 activated carbon electrodes in batch-mode and single-pass capacitive deionization,
597 Sep. Purif. Technol., 2019, 215, 403-409.
- 598 19 S. Zhao, J. S. Fang, Y. Y. Wang, Y. W. Zhang, Y. M. Zhou and S. P. Zhuo,
599 Construction of three-dimensional mesoporous carbon nitride with high surface area
600 for efficient visible-light-driven hydrogen evolution, J. Colloid Interface Sci., 2020,
601 561, 601-608.
- 602 20 J. S. Kang, S. Kim, J. H. Kang, H. Joo, J. Jang, K. Jo, S. Park, H. I. Kim, S. J. Yoo, J.
603 Yoon, Y. E. Sung and T. A. Hatton, Surface Electrochemistry of Carbon Electrodes
604 and Faradaic Reactions in Capacitive Deionization, Environ. Sci. Technol., 2022, 56,
605 12602-12612.
- 606 21 D. Lu, W. F. Cai and Y. Wang, Optimization of the voltage window for long-term
607 capacitive deionization stability, Desalination, 2017, 424, 53-61.
- 608 22 T. K. A. Nguyen, N. T. N. Anh, M. D. Nguyen, V. T. Nguyen and R. A. Doong,
609 Boosting capacitive deionization of monovalent and hardness ions using Ti₃C₂T_x
610 MXene as an intercalation-type pseudocapacitive electrode, Sep. Purif. Technol.,
611 2023, 327, 13.
- 612 23 S. W. Tsai, D. V. Cuong and C. H. Hou, Selective capture of ammonium ions from
613 municipal wastewater treatment plant effluent with a nickel hexacyanoferrate
614 electrode, Water Res., 2022, 221, 10.
- 615 24 Q. F. Wang, Q. H. Wu, S. J. Meng, H. J. Liu and D. W. Liang, Selective removal of
616 ammonium ions with transition metal hexacyanoferrate (MHCF) electrodes,
617 Desalination, 2023, 558, 9.
- 618 25 S. Q. Gong, H. B. Liu, F. Zhao, Y. N. Zhang, H. T. Xu, M. Li, J. J. Qi, H. H. Wang,
619 C. L. Li, W. C. Peng, X. B. Fan and J. P. Liu, Vertically Aligned Bismuthene
620 Nanosheets on MXene for High-Performance Capacitive Deionization, ACS Nano,
621 2023, 17, 4843-4853.
- 622 26 J. Yang, W. X. Hou, R. Pan, M. Zhou, S. Z. Zhang and Y. Zhang, The interfacial
623 electronic engineering in polyhedral MOF derived Co-doped NiSe₂ composite for
624 upgrading rate and longevity performance of aqueous energy storage, J. Alloy.
625 Compd., 2022, 897, 7.
- 626 27 Y. Lu, Q. Zhang, L. Li, Z. Q. Niu and J. Chen, Design Strategies toward Enhancing
627 the Performance of Organic Electrode Materials in Metal-Ion Batteries, Chem, 2018,
628 4, 2786-2813.
- 629 28 T. Sun, J. Xie, W. Guo, D. S. Li and Q. C. Zhang, Covalent-Organic Frameworks:
630 Advanced Organic Electrode Materials for Rechargeable Batteries, Adv. Energy
631 Mater., 2020, 10, 23.
- 632 29 J. J. Shea and C. Luo, Organic Electrode Materials for Metal Ion Batteries, ACS
633 Appl. Mater. Interfaces, 2020, 12, 5361-5380.
- 634 30 Y. H. Tao, Y. J. Cui, H. X. Wang, Z. L. Li, Z. J. S. Qian, P. P. Zhang, H. J. Zhou and
635 M. J. Shi, High-Efficiency Electrochemical Desalination: The Role of a Rigid
636 Pseudocapacitive Polymer Electrode with Diverse Active Sites, Adv. Funct. Mater.,
637 2025, 35, 11.
- 638 31 Z. Y. Zhuang, L. Sun, Y. H. Tao, J. Shao, J. G. Yang, P. Yu, H. X. Chen, J. H. Zhou,



- 639 J. Xiao, K. Y. Yin, M. J. Shi and P. Xiao, Highly Efficient and Stable Capacitive
640 Deionization Based on a Flower-Like Conjugated Polymer with Double Active-Sites,
641 *Energy Environ. Mater.*, 2024, 8, 9.
- 642 32 M. Quan, D. Sanchez, M. F. Wasylikiw and D. K. Smith, Voltammetry of quinones in
643 unbuffered aqueous solution: Reassessing the roles of proton transfer and hydrogen
644 bonding in the aqueous Electrochemistry of Quinones, *J. Am. Chem. Soc.*, 2007, 129,
645 12847-12856.
- 646 33 B. Schoepp-Cothenet, R. van Lis, A. Atteia, F. Baymann, L. Capowiez, A. L.
647 Ducluzeau, S. Duval, F. ten Brink, M. J. Russell and W. Nitschke, On the universal
648 core of bioenergetics, *Biochim. Biophys. Acta-Bioenerg.*, 2013, 1827, 79-93.
- 649 34 R. W. Jing, J. Yang, X. R. Zhao, Y. T. Wang, P. R. Shao, M. J. Shi and C. Yan, A
650 carbonyl-rich conjugated organic compound for aqueous rechargeable Na plus
651 storage with wide voltage window workability, *J. Colloid Interface Sci.*, 2024, 658,
652 678-687.
- 653 35 R. W. Jing, J. He, L. T. Hu, J. Yang, C. Yan and M. J. Shi, A holomolecule
654 conjugated and electron delocalized organic compound for superior proton-storage
655 redox capability, *Chem. Eng. J.*, 2023, 477, 9.
- 656 36 Y. Y. Ding, X. Ren, D. Chen, F. J. Wen, T. Li and F. Xu,
657 Poly(1,5-diaminoanthraquinone) as a High-Capacity Bipolar Cathode for
658 Rechargeable Magnesium Batteries, *ACS Appl. Energ. Mater.*, 2022, 5, 3004-3012.
- 659 37 X. G. Li, X. L. Ma and M. R. Huang, Lead(II) ion-selective electrode based on
660 polyaminoanthraquinone particles with intrinsic conductivity, *Talanta*, 2009, 78,
661 498-505.
- 662 38 T. Günther, K. Oka, S. Olsson, M. Åhlén, N. Tohnai and R. Emanuelsson, Redox-site
663 accessibility of composites containing a 2D redox-active covalent organic framework:
664 from optimization to application, *J. Mater. Chem. A*, 2023, 11, 13923-13931.
- 665 39 Z. Y. Meng, Y. Zhang, M. Q. Dong, Y. Zhang, F. M. Cui, T. P. Loh, Y. H. Jin, W.
666 Zhang, H. S. Yang and Y. Du, Readily useable bulk phenoxazine-based covalent
667 organic framework cathode materials with superior kinetics and high redox potentials,
668 *J. Mater. Chem. A*, 2021, 9, 10661-10665.
- 669 40 M. R. Huang, S. J. Huang and X. G. Li, Facile Synthesis of
670 Polysulfoaminoanthraquinone Nanosorbents for Rapid Removal and Ultrasensitive
671 Fluorescent Detection of Heavy Metal Ions, *J. Phys. Chem. C*, 2011, 115, 5301-5315.
- 672 41 F. L. Zhang, J. B. Fan and S. T. Wang, Interfacial Polymerization: From Chemistry to
673 Functional Materials, *Angew. Chem.-Int. Edit.*, 2020, 59, 21840-21856.
- 674 42 W. H. Shi, X. Y. Liu, T. Q. Deng, S. Z. Huang, M. Ding, X. H. Miao, C. Z. Zhu, Y.
675 H. Zhu, W. X. Liu, F. F. Wu, C. J. Gao, S. W. Yang, H. Y. Yang, J. N. Shen and X.
676 H. Cao, Enabling Superior Sodium Capture for Efficient Water Desalination by a
677 Tubular Polyaniline Decorated with Prussian Blue Nanocrystals, *Adv. Mater.*, 2020,
678 32, 9.
- 679 43 J. Jin, R. Y. Wang, K. Yu, Y. H. Tao, P. P. Zhang, L. Ke, J. Yang and M. J. Shi,
680 Imine-based conjugated polymer enables efficient removal of ammonium ion via
681 capacitive deionization, *Sep. Purif. Technol.*, 2025, 353, 9.
- 682 44 D. D. Chen, X. H. Yi, C. Zhao, H. F. Fu, P. Wang and C. C. Wang, Polyaniline



- 683 modified MIL-100(Fe) for enhanced photocatalytic Cr(VI) reduction and tetracycline
684 degradation under white light, *Chemosphere*, 2020, 245, 12.
- 685 45 T. Y. Liu, K. C. Kim, B. Lee, S. Jin, M. J. Lee, M. Li, S. Noda, S. S. Jang and S. W.
686 Lee, Enhanced Lithium Storage of an Organic Cathode via the Bipolar Mechanism,
687 *ACS Appl. Energ. Mater.*, 2020, 3, 3728-3735.
- 688 46 L. Lin, Z. R. Lin, J. Q. Zhu, K. Wang, W. L. Wu, T. Qiu and X. Q. Sun, A
689 semi-conductive organic cathode material enabled by extended conjugation for
690 rechargeable aqueous zinc batteries, *Energy Environ. Sci.*, 2023, 16, 89-96.
- 691 47 J. L. Liu and P. Liu, Well-defined poly(1,5-diaminoanthraquinone)/reduced graphene
692 oxide hybrids with superior electrochemical property for high performance
693 electrochemical capacitors, *J. Colloid Interface Sci.*, 2019, 542, 33-44.
- 694 48 S. J. Huang, C. G. Min, Y. Z. Liao, P. Du, H. Sun, Y. Q. Zhu and A. M. Ren,
695 Intrinsically conducting polyaminoanthraquinone nanofibrils: interfacial synthesis,
696 formation mechanism and lead adsorbents, *RSC Adv.*, 2014, 4, 47657-47669.
- 697 49 A. I. Drachev, A. B. Gil'man and A. A. Kuznetsov, Polymerization of anthracene in a
698 direct-current discharge, *High Energy Chem.*, 2005, 39, 418-419.
- 699 50 J. L. Ren, X. Zhao, J. X. Zhang and Q. H. Zhang, Anthraquinone Immobilized on
700 Reduced Graphene Oxide Sheets with Improved Electrochemical Properties for
701 Supercapacitors, *Int. J. Electrochem. Sci.*, 2016, 11, 2550-2559.
- 702 51 E. Jocar, S. Shahrokhian and A. I. Zad, Electrochemical functionalization of graphene
703 nanosheets with catechol derivatives as an effective method for preparation of highly
704 performance supercapacitors, *Electrochim. Acta*, 2014, 147, 136-142.
- 705 52 A. A. Zhang, Z. X. Wang, Z. B. Fang, J. L. Li and T. F. Liu, Long-Range π - π
706 Stacking Brings High Electron Delocalization for Enhanced Photocatalytic Activity
707 in Hydrogen-Bonded Organic Framework, *Angew. Chem.-Int. Edit.*, 2024, 63, 8.
- 708 53 P. P. Yu, Y. Z. Li, X. Y. Yu, X. Zhao, L. H. Wu and Q. H. Zhang, Polyaniline
709 Nanowire Arrays Aligned on Nitrogen-Doped Carbon Fabric for High-Performance
710 Flexible Supercapacitors, *Langmuir*, 2013, 29, 12051-12058.
- 711 54 X. R. Zhao, J. Yang, J. Y. Peng, Y. Liu, H. Zhang, C. Yan and M. J. Shi, An extended
712 S-heterocyclic organic compound with enhanced redox active sites for efficient and
713 stable ammonium ion removal via capacitive deionization, *Desalination*, 2024, 592,
714 11.
- 715 55 Y. H. Tao, J. Jin, X. Y. Zhang, Z. J. S. Qian, J. T. Jiang and M. J. Shi, A tailored
716 polymer with enhanced electrosorption capability for efficient ammonium removal,
717 *Sep. Purif. Technol.*, 2025, 362, 8.
- 718 56 D. Jiang, R. B. Xu, L. Bai, J. P. Hill, J. Henzie, L. Y. Zhu, W. Xia, R. Bu, Y. J. Zhao,
719 Y. Q. Kang, T. Hamada, R. Z. Ma, N. Torad, J. Wang, T. Asahi, X. T. Xu and Y.
720 Yamauchi, Substrate Curvature-Induced Regulation of Charge Distribution of
721 Covalent Organic Frameworks Promotes Capacitive Deionization, *Adv. Funct.*
722 *Mater.*, 2024, 34, 10.
- 723 57 R. Y. Wang, J. He, C. Yan, R. W. Jing, Y. Zhao, J. Yang, M. J. Shi and X. B. Yan, A
724 Long-Range Planar Polymer with Efficient π -Electron Delocalization for Superior
725 Proton Storage, *Adv. Mater.*, 2024, 36, 12.
- 726 58 Q. Che, C. Y. Li, Z. H. Chen, S. Yang, W. F. Zhang and G. Yu, High Performance



- 727 Memristors Based on Imine-Linked Covalent Organic Frameworks Obtained Using a
728 Protonation Modification Strategy, *Angew. Chem.-Int. Edit.*, 2024, 63, 9. View Article Online
DOI: 10.1039/D6TA02416E
- 729 59 J. He, Y. Zhao, C. Yan, R. W. Jing, R. Y. Wang and M. J. Shi, Highly redox-active
730 polymer with extensive electron delocalization and optimized molecular orbitals for
731 extraordinary proton storage, *Chem. Eng. J.*, 2023, 470, 8.
- 732 60 T. Brezesinski, J. Wang, S. H. Tolbert and B. Dunn, Ordered mesoporous α -MoO₃
733 with iso-oriented nanocrystalline walls for thin-film pseudocapacitors, *Nat. Mater.*,
734 2010, 9, 146-151.
- 735 61 R. Y. Wang, M. J. Shi, L. Y. Li, Y. Zhao, L. P. Zhao and C. Yan, In-situ investigation
736 and application of cyano-substituted organic electrode for rechargeable aqueous
737 Na-ion batteries, *Chem. Eng. J.*, 2023, 451, 10.
- 738 62 Y. F. An, H. Zhang, D. X. Geng, Z. J. Fu, Z. M. Liu, J. He, Y. Zhao, M. J. Shi and C.
739 Yan, Double redox-active polyimide-based covalent organic framework induced by
740 lithium ion for boosting high-performance aqueous Zn²⁺ storage, *Chem. Eng. J.*,
741 2023, 477, 9.
- 742 63 W. W. Ji, J. J. Niu, W. Zhang, X. Li, W. J. Yan, X. G. Hao and Z. D. Wang, An
743 electroactive ion exchange hybrid film with collaboratively-driven ability for
744 electrochemically-mediated selective extraction of chloride ions, *Chem. Eng. J.*,
745 2022, 427, 11.
- 746 64 R. Vedalakshmi, V. Saraswathy, H. W. Song and N. Palaniswamy, Determination of
747 diffusion coefficient of chloride in concrete using Warburg diffusion coefficient,
748 *Corrosion Sci.*, 2009, 51, 1299-1307.
- 749 65 H. Sakar, O. Karatas, C. B. Canbolat, B. Keskinler and A. Karagunduz, Removal of
750 ammonium ions by capacitive deionization and membrane capacitive deionization
751 units, *Desalin. Water Treat.*, 2017, 75, 260-267.
- 752 66 O. Pastushok, D. L. Ramasamy, M. Sillanpää and E. Repo, Enhanced ammonium
753 removal and recovery from municipal wastewater by asymmetric CDI cell equipped
754 with oxygen functionalized carbon electrode, *Sep. Purif. Technol.*, 2021, 274, 13.
- 755



A Data Availability Statement

View Article Online
DOI: 10.1039/D6TA02416E

The data that support this study will be shared upon reasonable request to the corresponding author.

